UNIVERSITATEA “BABEŞ-BOLYAI” CLUJ-NAPOCA

FACULTATEA DE FIZICĂ

SPECIALIZAREA FIZICĂ COMPUTAȚIONALĂ

LUCRARE DE DISERTAȚIE

Coordonator științific

Conf. Dr. András Libál

Absolvent

Péter Forgacs

[2023]

UNIVERSITATEA “BABEŞ-BOLYAI” CLUJ-NAPOCA

FACULTATEA DE FIZICĂ

SPECIALIZAREA FIZICĂ COMPUTAȚIONALĂ

LUCRARE DE DISERTAȚIE

S-I-R MODEL ON ACTIVE MATTER

Coordonator științific

Conf. Dr. András Libál

Absolvent

Péter Forgacs

[2023]

ABSTRACT

This study investigates the dynamics of epidemics in a heterogeneous environment using simulations of active matter particles. The susceptible-infected-recovered (S-I-R) model is integrated into the active matter system, considering variations in the infection and recovery rates. The effects of introducing quenched disorder in the form of immobile obstacles are also explored. The results show that the presence of quenched disorder increases the occurrence of failed outbreaks and prolongs successful epidemics, particularly at low infection rates. In contrast, at high infection rates, the system becomes less sensitive to quenched disorder and exhibits well-defined spatial fronts. The study suggests that the assumption of homogeneous mixing breaks down in the presence of quenched disorder, highlighting the importance of spatial heterogeneity in epidemic dynamics. The potential for experimental realization using light-activated colloids is discussed, offering a tabletop approach to model epidemic spreading with active matter. The research has been published in *Scientific Reports* (citation: [11]).

Contents

Introduction

The spread of diseases in a diverse environment has gained global attention. Extensive modeling efforts have been dedicated to controlling or predicting the progression of the pandemic. Most of these models are based on the susceptible-infected-removed (S-I-R) model introduced by Kermack and McKendrick [17] almost a century ago. In this model, the population is divided into susceptible (S), infected (I), and recovered (R) individuals, and the epidemic's dynamics are governed by transition rates between these categories. In a specific group, individuals cannot be differentiated, and any spatial characteristics of the system are disregarded [29]. Although S-I-R models and their numerous variations may seem straightforward, they offer robust capabilities for predicting the overall trajectory of an epidemic. However, these models struggle to predict the specific course of real-world epidemics due to the heterogeneity in individual susceptibility, spatial contacts, and mixing behaviors [15], leading to unpredictable stochastic effects.

In this study, simulations of a large collection of active matter particles within the MIPS regime were conducted, leading to the spontaneous formation of a giant cluster. This model is integrated with S-I-R interactions, where all particles initially fall into the susceptible (S) category but have a probability β of becoming infected upon direct contact with an infected (I) particle. Infected particles then transition spontaneously to the recovered (R) state at a rate μ, with no possibility of reinfection. The investigation focuses on the evolution of epidemics by varying the ratio of β/μ, while also exploring the effects of introducing quenched disorder in the form of immobile obstacles. As the number of immobile obstacles increases in the active matter system, the number of clusters grows while their sizes decrease. Through numerous realizations, we observe that the inclusion of quenched disorder amplifies the occurrence of "failed" outbreaks for small β/μ ratios and prolongs the average duration of successful epidemics. When β/μ is sufficiently large, the system becomes less sensitive to the presence of quenched disorder, approaching the mean field limit where the epidemic propagates through well-defined spatial fronts. Furthermore, we investigate the average number of susceptible particles surrounding an infective over time and find that this metric undergoes moderate changes due to the addition of quenched disorder in the high β/μ mean field limit, but experiences significant alterations as quenched disorder is introduced with lower β/μ ratios.

The findings suggest that at low β/μ ratios, the assumption of homogeneous mixing no longer holds true, indicating a departure from mass action in the infection process. In such

cases, the system becomes highly sensitive to spatial quenched disorder. On the other hand, in the high β/μ regime, although the epidemic spreads through spatially localized fronts, the mixing hypothesis remains more applicable. This implies that localized interventions to mitigate the epidemic would be more effective at low β/μ ratios but would lose effectiveness in higher β/μ regimes unless implemented across the entire population.

Lastly, we explore the potential experimental realization of our system by employing feedback control of light-activated colloids, allowing for individual-level control over the colloids' active behavior. Previous experiments involving such systems have successfully demonstrated group formation, responsive states, and the implementation of predator-prey models [1,7,19]. Furthermore, there exist various approaches to introduce spatial heterogeneities in active matter systems [3, 20, 26, 32, 35, 39]. By leveraging these techniques, it becomes possible to mimic the S-I-R model, both with and without spatial disorder, creating tabletop models of epidemic spreading using active matter.

This work is already published in *Scientific Reports* [11] (see the citation).

Chapter 1

Description of the field

This chapter provides insights into active matter, S-I-R models, and motivates the use of active matter for modeling the spread of diseases. There is also a description of molecular dynamics simulations, because this study was also realised by performing simulations.

1.1 Active matter

A review by Bechinger et al. [2] describes the properties of active matter and it's differences from simple Brownian particles very well:

Active matter systems possess the remarkable ability to extract energy from their surroundings and exist far from thermal equilibrium. This unique characteristic gives rise to a range of intriguing phenomena that are inaccessible to equilibrium matter, such as collective swarming and the emergence of collective properties. Exploring active matter offers exciting prospects for uncovering new physics and developing innovative strategies for designing intelligent devices and materials. In recent years, there has been a significant and growing effort to advance this field and explore its applications across various disciplines, including statistical physics, biology, robotics, social transport, soft matter, and biomedicine.

One prominent example of active matter consists of natural and artificial entities capable of self-propulsion. Initially, self-propelled particles were studied to model the collective behavior of animal swarms at a macroscopic scale. The "Boids model" simulated the aggregate motion of bird flocks, land animal herds, and fish schools in computer graphics applications. Later the Vicsek model was introduced as a specific case. In the Vicsek model, a swarm is represented by a collection of self-propelling particles that move at a constant speed while tending to align with the average direction of motion of nearby particles in their local vicinity. Swarming systems exhibit emergent behaviors at various scales, some of which are robust and universal, independent of the specific types of animals constituting the swarm. Consequently, a challenge for theoretical physics has been to develop minimal statistical models capable of capturing these characteristics.

1.2 Susceptible-Infected-Recovered model

The S-I-R model [15, 17] is a widely used mathematical framework for studying the spread of infectious diseases within a population. It divides the population into three distinct compartments: Susceptible (S), Infected (I), and Recovered (R).

- Susceptible (S): Individuals in this compartment are susceptible to contracting the disease. They have not been infected before and can become infected if they come into contact with infectious individuals.
- Infected (I): Individuals in this compartment are currently infected with the disease. They can transmit the infection to susceptible individuals through direct contact or other means of transmission.
- Recovered (R): Individuals in this compartment have recovered from the infection and are now immune to it. They cannot be reinfected and do not contribute to the further spread of the disease.

The S-I-R model assumes that the total population remains constant over time and that individuals move between these compartments based on certain rates. Typically, the transition from the susceptible to the infected state occurs at a rate determined by the infection rate (β), representing the likelihood of transmission per contact between susceptible and infected individuals. The transition from the infected to the recovered state occurs at a rate determined by the recovery rate (μ), representing the average duration of the infection.

By analyzing the dynamics of these transitions, the SIR model provides insights into the progression and control of epidemics, such as the peak infection rate, the total number of infections, and the effectiveness of interventions like vaccination or social distancing measures.

1.3 Molecular dynamics simulation

Molecular dynamics (MD) simulations [13, 33] are computational methods used to study the behavior and interactions of atoms and molecules over time. They simulate the movement and interactions of particles by solving the equations of motion derived from classical mechanics or quantum mechanics, depending on the level of detail required.

In molecular dynamics simulations, the atoms or molecules in a system are represented as particles, and their positions, velocities, and forces are tracked as the simulation progresses. The behavior of the system is determined by the interatomic or intermolecular potential energy function, which describes the forces between the particles. This potential energy function accounts for various types of interactions, such as bond stretching, angle bending, van der Waals forces, and electrostatic interactions.

The simulation starts with an initial configuration of the system, typically obtained from experimental data or by generating a random arrangement of particles. The equations of

motion are then numerically integrated to update the positions and velocities of the particles over small time steps. This iterative process is repeated for a desired duration, allowing the system to evolve dynamically.

Molecular dynamics simulations can provide valuable insights into the behavior and properties of materials at the atomic or molecular level. They can reveal information about thermodynamic properties, phase transitions, chemical reactions, diffusion processes, and other dynamical phenomena. By varying simulation parameters, such as temperature, pressure, or composition, researchers can explore the effect of different conditions on the system's behavior.

MD simulations have broad applications in various fields, including chemistry, materials science, biology, and physics. They are used to study diverse systems such as liquids, solids, proteins, nucleic acids, polymers, nanoparticles, and complex biomolecular assemblies. The results obtained from MD simulations can complement experimental observations, guide the design of new materials, and provide detailed atomistic understanding of molecular processes that are difficult to probe experimentally.

1.4 State of the art

To address the challenge of heterogeneity, various approaches have been developed. One approach involves dividing the population into subpopulations with different infection and recovery rates or subdividing it geographically into regions with diffusive terms [9,16]. Patchiness can also be incorporated to introduce additional heterogeneities [18, 40]. Extensive research has been conducted on linking individuals through finite-dimensional networks instead of an infinite-dimensional mean field [29]. However, the intricacies of the network introduce further complexity to the problem, as decisions need to be made regarding the suitable degree distribution for network connectivity. Additionally, determining whether the network should remain static or evolve independently or in response to the disease's progression [36, 44] adds to the complexity. The impact of heterogeneity in transmission and susceptibility has been extensively discussed [23].

Agent-Based Modeling (ABM) or Individual Based Modeling [21] provides a more detailed approach by treating each individual as a separate, interacting unit. ABM allows for heterogeneity at different levels, including individual susceptibility, contact patterns, spatial clustering, and short/long-range transportation [8,14]. However, ABM models face challenges in computational complexity and the calibration of numerous parameters with limited real-world data.

Efforts to find a middle ground in ABM, where some details are abstracted while capturing meaningful spatial heterogeneity, have surprisingly been limited. This balance can be achieved by either developing more intricate analytical models or simpler simulation-based models. One of the earliest approaches to simplify simulation-based models was through the use of cellular automata, allowing for varied mobility of individual agents within the mean-

field limit [4]. Individuals following S-I-R interactions have also been represented as moving particles with characteristics such as driven diffusion [12], unidirectional movement [30], occasional long-range jumps [5], different velocities [38], or confinement to specific regions [42]. To alleviate the computational burden associated with such methods, dynamic density functional theory techniques can be employed [41].

Recent advancements in active matter models [2,22], which involve self-propelled particles interacting on a spatial landscape with or without disorder, have opened up new possibilities for combining them with S-I-R type models. These active particles can exhibit behaviors such as run-and-tumble [31] or driven diffusion [28]. In specific cases, a low-density active matter system was able to replicate the mean field behavior of S-I-R [25]. However, there has been limited research on integrating S-I-R modeling with active matter in general. For instance, Paoluzzi et al. explored S-I-R dynamics to investigate information exchange during active clustering transitions [28] but did not focus on the actual spreading of the epidemic. More recently, Zhao et al. examined contagion dynamics in self-propelled flocking models and discovered that ordered homogeneous states hinder disease spreading, while bands and clustering promote it [45].

Working with an active matter system offers several advantages. The well-known motility-induced phase separation (MIPS) transition, where a low-density gas phase transforms into coexisting high and low density regions based on the density and mobility of active particles [6, 10, 27, 34], naturally separates particles into clustered communities connected by disordered transport pathways. The interactions between particles can be seen as an adaptive network that can be adjusted to evolve on the same or different time scales as the disease progresses. Spatial heterogeneity arises organically within the MIPS regime, but it can also be introduced using walls, traps, or obstacles. Disease dynamics in such systems can be represented by monitoring the temporal evolution of the number of susceptible ($S(t)$), infected ($I(t)$), and recovered ($R(t)$) individuals over time, capturing the effects of heterogeneities that are averaged out in the mean field approximations of the standard S-I-R model.

Chapter 2

The simulation

The simulation was written in C, and is performed on a two-dimensional system with a size of $L \times L$, where $L = 200$, and periodic boundary conditions are applied in both the x and y directions. The system consists of $N = 5000$ active particles.

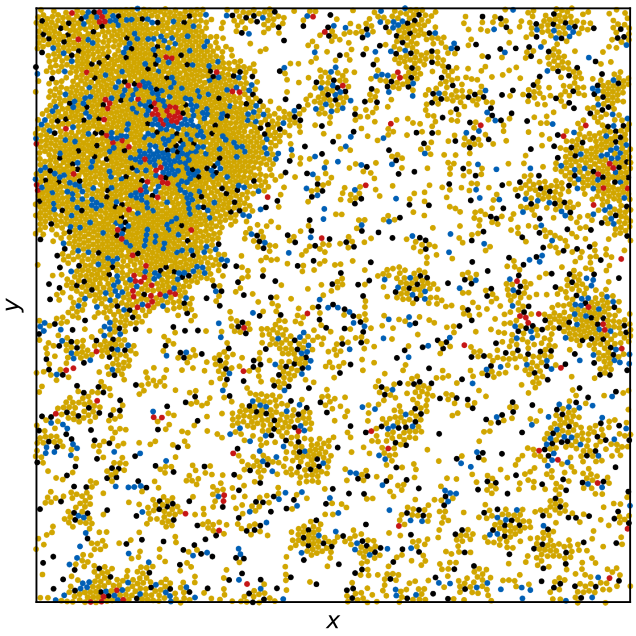

Figure 2.1: The depicted image illustrates a sample comprising run-and-tumble S-I-R particles in a regime of motility-induced phase separation. The particles undergo transitions between susceptible (S, represented in yellow), infected (I, represented in red), and recovered (R, represented in blue) states. In this case, the ratio of β/μ is 0.5. Additionally, there is the presence of quenched disorder in the form of $N_{\text{obs}} = 800$ immobile obstacles (depicted in black). This quenched disorder leads to the formation of numerous small clusters alongside the prominent motility-induced phase separation (MIPS) cluster.

2.1 Equation of motion

The movement of the particles is determined by numerically integrating the following equation over discrete time steps ($\Delta t = 0.005$):

$$\alpha_d \mathbf{v}_i = \mathbf{F}_i^{dd} + \mathbf{F}_i^{m} + \mathbf{F}_i^{\text{obs}} \tag{2.1}$$

, where $\alpha_d = 1.0$ is the damping constant, $\mathbf{v}_i = \frac{\mathrm{d}\mathbf{r}_i}{\mathrm{d}t}$ is the velocity and $\mathbf{r}_i$ is the position of particle i. $\mathbf{F}_i^{dd} = \sum_{i \neq j}^{N} k(2r_a - |\mathbf{r}_{ij}|)\Theta(2r_a - |\mathbf{r}_{ij}|)\hat{\mathbf{r}}_{ij}$ is the harmonic repulsive potential interaction between two particles, where Θ if the Heaviside step function, $k = 20$ is the spring force, $r_a = 1.0$ is the radius of a particle, $\mathbf{r}_{ij} = \mathbf{r}_i - \mathbf{r}_j$ and $\hat{\mathbf{r}}_{ij} = \mathbf{r}_{ij}/|\mathbf{r}_{ij}|$.

Each particle has a motor force $\mathbf{F}_i^m = F_M \hat{\mathbf{m}}_i$, where F_M is the magnitude of the force and $\hat{\mathbf{m}}_i$ represents a randomly selected direction. This motor force acts on the particle for a duration of τ_l, after which the particle instantaneously changes its direction to another randomly chosen direction, creating a run-and-tumble behavior. The duration τ_l for each particle is randomly chosen after each change in direction from the range 1.5×10^4 to 3.0×10^4 simulation time steps. The motor force F_M is set to 1.5 for susceptible and recovered particles, creating the motility-induced phase separated (MIPS) regime in the absence of quenched disorder [39]. Infected particles have their motor force reduced to $F_M = 1.0$.

In some simulations, we introduce quenched disorder in the form of N_{obs} obstacles, which exert the force $\mathbf{F}^{\text{obs}}$. The force between particles and obstacles is the same as the particle-particle interaction force, but the obstacles remain immobile. Figure 2.1 shows an image of the system with obstacles.

2.2 S-I-R model dynamics and state transitions

The active particles in the system are categorized into three states: S (susceptible), I (infected), or R (recovered). When an S particle directly interacts with an I particle, there is a probability β that the S particle transitions to the I state for each simulation time step that the contact persists. If an S particle is in contact with n I particles at a given time step, the probability of infection is approximately $n\beta$, calculated as $1-(1-\beta)^n$. Transitions from the I state to the R state occur with a probability of μ at each simulation time step, independent of the state of other particles in contact with the I particle. Consequently, the mean duration of the infected state is $1/\mu$ simulation time steps.

The R state is absorbing, and particles in the R state do not undergo further state transitions. In this S-I-R model, the infected I particles are only transient, and the system will eventually consist of only S and/or R particles.

It is important to note that the mean-field rates governing S→I and I→R transitions, as well as determining the basic reproductive number R_0 in classical S-I-R models, do not directly correspond to the values of β and μ used as microscopic parameters in our model. In agent-based models (ABMs), the effective mean-field rates emerge as quantities rather than

being predefined parameters.

2.3 Initialization

To initialize the system, the particles are randomly distributed throughout the sample and all particles are assigned to the susceptible (S) state. The system is allowed to evolve for 5×10^5 simulation time steps until a stable giant cluster emerges in the motility-induced phase separated (MIPS) regime. This state is considered the initial condition at $t = 0$. Subsequently, 5 particles are randomly selected and their state is changed to infected (I). These particles serve as the index cases, deliberately choosing 5 instead of 1 to reduce the likelihood of a failed outbreak.

For setting the parameters of the simulations, so called parameter files (see the following subsection 2.3.1) are used.

2.3.1 Parameter file

To be able to run simulations with different parameters, the simulation needs a parameter file as input. The parameter file has the following structure:

```
SX 200.0
SY 200.0
N_particles 5000
N_obstacles 0
dt 0.005
total_runtime 500000
echo_time 1000
movie_time 5000
generic_particle_R 1.0
generic_particle_k_spring 20.0
generic_particle_motor_minimum_time 15000
generic_particle_motor_force 1.5
generic_Iparticle_motor_force 1.0
generic_obstacle_R 1.0
number_of_initial_I 5
beta 0.000008
mu 0.00002
seedToSet 0
```

More about the parameters:

- The `SX` and the `SY` parameters define the size of the system in the x and y directions respectively.

- The `N_particles` and the `N_obstacles` define the number of particles and the number of obstacles in the system.

- The `dt` defines the size of one simulation time steps. The `total_runtime` defines the number of simulation time steps to run before initializing the I particles.

- The `echo_time` defines after how many simulation time steps should the program write to the console, and after how many simulation time steps should the measures be saved into a file. The `movie_time` defines after how many time steps should the program write the coordinates and the details of the particles into the movie file.

- The `generic_particle_R` defines the radius of a particle, the `generic_particle_k_spring` defines the spring force of the particle, the `generic_particle_motor_minimum_time` defines the lower limit of τ_l (the upper limit is the double of the lower limit), the `generic_particle_motor_force` defines the size of the motor force vector for the S and R particles, the `generic_Iparticle_motor_force` defines the size of the motor force vector for the I particles, the `generic_obstacle_R` defines the radius of the obstacles.

- The `number_of_initial_I` defines the number of randomly selected S particles to turn into I, the `beta` defines the value of the S→I probability, the `mu` defines the I→R probability.

- The `seedToSet` defines the random seed used for random number generation.

2.4 Optimizations

Verlet lists [43], named after Loup Verlet, are a commonly used algorithmic technique in molecular dynamics simulations to efficiently compute pairwise interactions between particles. They are particularly useful in simulations involving large systems with many interacting particles, such as the system in this study.

The basic idea behind Verlet lists is to create a spatial data structure that stores information about the neighboring particles for each particle in the system. This data structure is constructed based on a cutoff distance, which determines the maximum distance at which particles can interact with each other. The construction of Verlet lists typically involves two main steps: initialization and updating.

During the initialization step, the Verlet lists are created by iterating over all particles in the system and identifying their neighboring particles within the specified cutoff distance. This process involves calculating the distances between particles and storing the relevant information in the lists.

Once the Verlet lists are initialized, they are updated at regular intervals or whenever particles move a significant distance. The update process involves checking whether any

particles have moved outside the current neighboring region or entered the region of other particles. If particles have moved beyond a certain threshold distance, the Verlet lists are reconstructed to include the updated set of neighboring particles.

The main advantage of Verlet lists is that they reduce the number of pairwise interactions that need to be computed in each simulation time step. Instead of evaluating interactions between all pairs of particles in the system, Verlet lists allow for a more selective approach by considering only the particles within the cutoff distance. This leads to significant computational savings, especially in systems with low particle density or when the interactions are short-ranged.

However, it is important to note that Verlet lists introduce some overhead due to the need for list construction and updating. The choice of the cutoff distance also requires careful consideration, as a too small value may result in missing interactions, while a too large value may reduce the efficiency gained from using Verlet lists.

The procedure for computing interactions between particles and obstacles differs from that of particle-particle interactions. To handle the obstacle interactions, we adopt a grid-based approach with a fixed grid spacing. Each obstacle is placed within the cell that contains its center, forming a grid structure. Each grid cell can accommodate one or more obstacles, as needed. This approach is feasible because the obstacles remain stationary after initialization.

To calculate the forces exerted on a particle by the obstacles, we first determine the grid cell that contains the particle's center. We then consider interactions between the particle and all the obstacles present in the current cell, as well as those in neighboring cells. By examining the obstacles within these cells, we can accurately compute the forces acting on the particle due to the obstacles.

Chapter 3

Data processing

The system undergoes continuous evolution involving particle motion and state reactions (S, I, R) until there are no more infected (I) particles present. We conduct 1000 realizations for each set of parameters.

Due to the considerable variation in the duration $t_d = \min\{t > 0 : I(t) = 0\}$ of individual epidemics, as demonstrated in the results (Chapter 4), we express time using the scaled quantity $\tilde{t} = t/t_d$. Using scaled time, we analyze epidemic curves $s(\tilde{t}) = S(\tilde{t})/N$, $i(\tilde{t}) = I(\tilde{t})/N$, and $r(\tilde{t}) = R(\tilde{t})/N$ to visually compare epidemic progression across different β/μ ratios.

Additionally, we measure the peak infective fraction $i_{\max}$ and the final susceptible fraction s_∞, which are commonly used indicators of epidemic severity.

To gain insights into the spatial dynamics of the system, we calculate the average number of susceptible particles surrounding an infective, $\eta(\tilde{t}) = I^{-1}(\tilde{t}) \sum_i^{I(\tilde{t})} \sum_j^{S(\tilde{t})} \mathbb{I}(|r_{ij}(\tilde{t})| = 2r_a)$, where $\mathbb{I}$ represents the indicator function and the sums over i and j encompass infected and susceptible particles, respectively. In a two-dimensional system with particles of identical radii r_a, the maximum coordination number is $z = 6$. When infected individuals are well-mixed, the average number of susceptible particles surrounding an infective, $\eta(\tilde{t})$, is proportional to $S(\tilde{t})$; specifically, $\eta(\tilde{t}) \propto z_c S(\tilde{t})/N$, where z_c denotes the average coordination number of the particles. Deviations from this behavior indicate a departure from the assumption of homogeneous mixing.

3.1 Creating plots

The data obtained from the simulation code written in C was saved in data files. These data files were then processed using Python, which was also utilized for generating plots and snapshots.

Due to the large number of realizations, the data processing was automated.

Chapter 4

Results

4.1 Low transmissibility regime

Figure 4.1a presents a snapshot of the system in the low transmissibility regime ($\beta/\mu = 0.5$) without quenched disorder. The particles in motion exhibit a phase-separated state, with a high density solid region and a low density gas region. As mentioned earlier, the relationship between β/μ and the basic reproductive number is an emergent quantity.

Within a cluster, where the expected number of contacts is $z = 6$, an index case is expected to generate approximately $\eta = 3$ secondary cases, indicating that the epidemic will infect a fraction of the cluster. However, if the index case originates in the gas phase, its expected number of contacts is likely $z < 1$, resulting in a reproductive number less than one and limited transmissions between clusters.

Figure 4.1d depicts the system with randomly positioned obstacles ($N_{\text{obs}} = 800$). In this configuration, the giant dense cluster is accompanied by several smaller persistent clusters that have formed around certain obstacle locations. Due to the interconnectedness of particles within each cluster, the assumption of homogeneous mixing breaks down for the epidemic dynamics within these clusters.

Consequently, by manipulating the number and size of the clusters, we can investigate various deviations from the mixing assumption. This allows us to explore a spectrum of scenarios, ranging from a single large cluster with minimal mixing to situations with an increased number of clusters and smaller sizes, leading to greater mixing.

Figures 4.1a–c demonstrate the temporal evolution of the susceptible (S), infected (I), and recovered (R) particles in the obstacle-free system at time points $\tilde{t} = 0.2$, 0.3, and 0.4. Conversely, Figures 4.1d–f display the evolution in the system that includes $N_{\text{obs}=800}$ obstacles. In both cases, when the infective particles come into contact with the giant cluster, the disease propagates within the cluster. However, due to the low probability of transmission, not all susceptible particles surrounding an infective particle become infected.

Consequently, there are still a finite number of susceptible particles remaining once the epidemic concludes. The presence of quenched disorder, represented by black circles in Figures 4.1d–f, results in increased localized clustering in addition to the giant cluster. Since

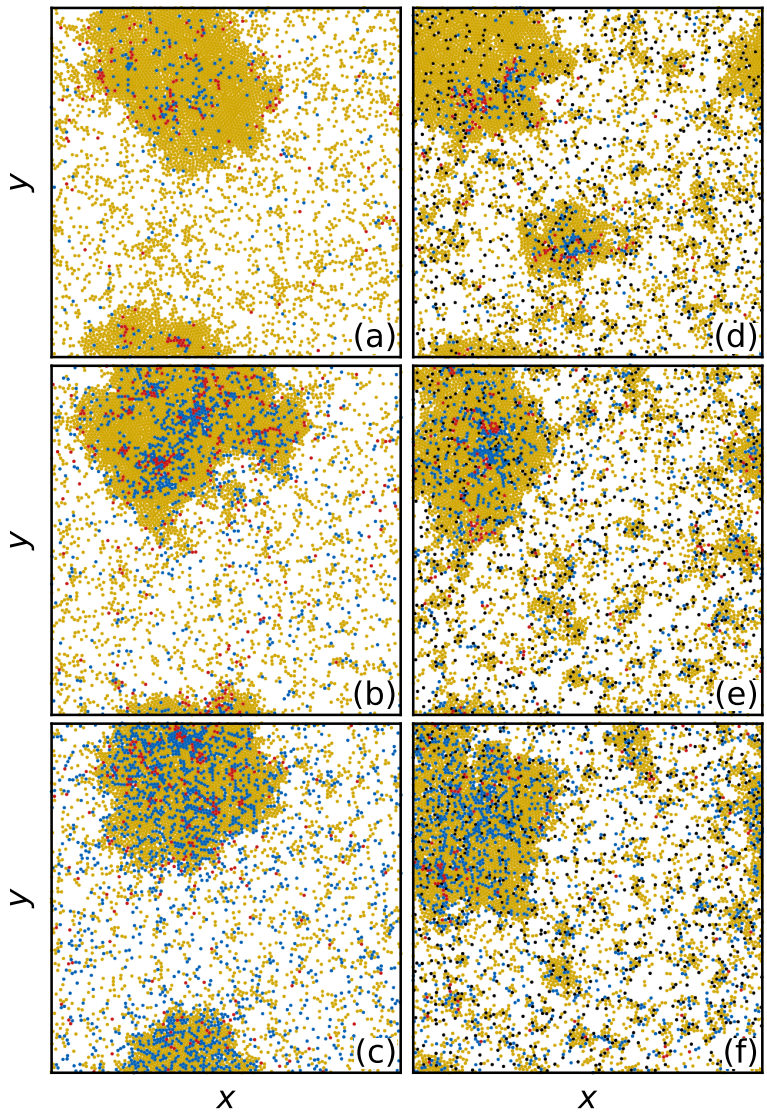

Figure 4.1: Illustrations showcasing the low transmissibility regime with and without quenched disorder are presented. The progression of the epidemic in the system depicted in Figure 1, with $\beta/\mu = 0.5$, is observed at timepoints (a,d) $\tilde{t} = 0.2$, (b,e) $\tilde{t} = 0.3$, and (c,f) $\tilde{t} = 0.4$. The particles exhibit transitions between susceptible (S, yellow), infected (I, red), and recovered (R, blue) states. Panels (a–c) represent the system without obstacles, while panels (d–f) depict the system containing obstacles ($N_{\text{obs}} = 800$). It can be observed that the presence of obstacles results in fewer infected particles at later time instances.

each cluster must be infected individually, this slows down the spread of the infection and reduces the peak infective fraction (i_{max}), as depicted in Figure 4.1e. For further insights into the final epidemic size, refer to Ref. [24].

While the dynamics of infection spread show similarities in the presence and absence of quenched disorder, there is a notable difference at $\tilde{t} = 0.4$. In the system where obstacles have fragmented the system into smaller clusters, the number of infected (I) particles is significantly lower. This suggests that the epidemic has affected a smaller proportion of particles in the system with quenched disorder.

Figure 4.2a displays the epidemic curves, representing the fractions of susceptible (s), infected (i), and recovered (r) particles as a function of scaled time ($\tilde{t}$), for samples with

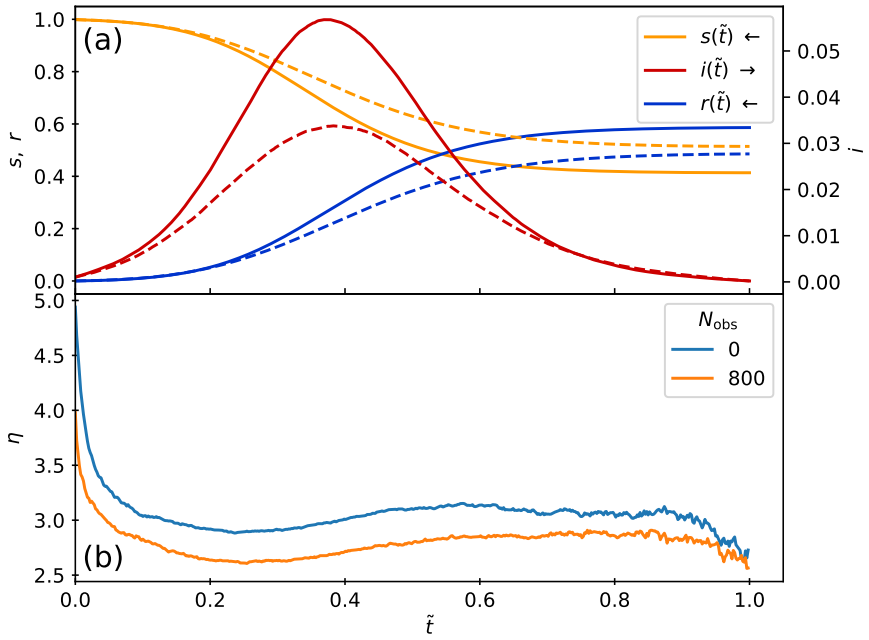

Figure 4.2: Epidemic curves in the low transmissibility regime are displayed. In panel (a), the fractions of susceptible (s, yellow), infected (i, red), and recovered (r, blue) particles are plotted against rescaled time $\tilde{t}$ for the system shown in Figure 4.1 with $\beta/\mu = 0.5$. Solid lines represent samples without quenched disorder, while dashed lines correspond to samples containing obstacles ($N_{\text{obs}} = 800$). At $\tilde{t} = 1.0$, the epidemic concludes with $i = 0$. The introduction of obstacles diminishes the peak value $i_{\max}$ of the infective curve. In panel (b), the corresponding η, which denotes the average number of S particles surrounding an I particle, is depicted against $\tilde{t}$ for the sample without obstacles (blue) and the sample with obstacles (orange). The inclusion of obstacles significantly reduces η throughout the entire epidemic.

and without quenched disorder. It is worth noting that the presence of obstacles tends to prolong the duration of the epidemic. However, by plotting the epidemic curves in terms of scaled time, it becomes easier to compare samples with and without quenched disorder. The curves exhibit the expected patterns characteristic of the classic S-I-R model.

In the absence of obstacles, at the end of the epidemic, a fraction $s_\infty = 0.41$ of the population remains uninfected, while $r_\infty = 1 - s_\infty = 0.59$ of the particles have recovered. Conversely, when obstacles are present, a larger fraction $s_\infty = 0.51$ of particles have avoided infection. Moreover, the peak value $i_{\max}$ in the infected fraction is significantly reduced in magnitude when obstacles are introduced. This suggests that the system is sensitive to the spatial heterogeneities introduced by the clustering resulting from the fixed obstacles. Within this regime, localized mitigation protocols that target specific spatial regions could be effective, as the presence of local quenched disorder can impede overall particle mobility or diminish effective particle connectivity.

To further illustrate the impact of obstacles, Figure 4.2b portrays η, the average number of susceptible (S) particles surrounding an infected (I) particle, as a function of scaled time. In the sample containing obstacles, η consistently exhibits smaller values compared to the

sample without obstacles.

4.2 High transmissibility regime

We now examine the scenario of high transmissibility with $\beta/\mu = 5.0$. Figure 4.3a–c depict the spatial progression of susceptible, infected, and recovered particles in the absence of obstacles. The infection spreads through distinct fronts that propagate within the dense region.

Conversely, Figure 4.3d–f illustrate the same evolution in the presence of obstacles ($N_{\text{obs}} = 800$). In this case, multiple dense clusters are observed, but each cluster exhibits a similar pattern of front propagation for the infection.

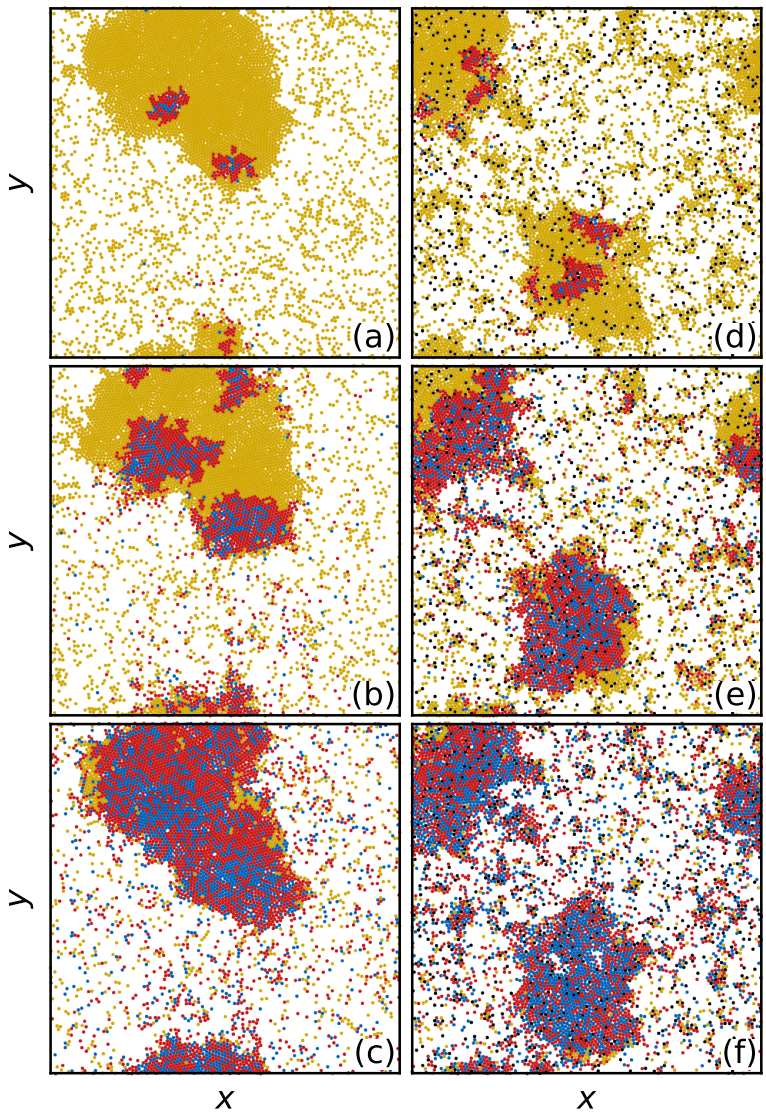

Figure 4.3: Panels (a–c) depict the evolution of the epidemic in the high transmissibility regime for systems without quenched disorder, with $\beta/\mu = 5.0$. The snapshots correspond to times $\tilde{t} = 0.1$ (a,d), 0.2 (b,e), and 0.3 (c,f). The particles, representing susceptible (S), infected (I), and recovered (R) states, transition between these states. Similarly, panels (d–f) illustrate the evolution of the epidemic in the presence of obstacles ($N_{\text{obs}} = 800$). In both cases, the epidemic propagates as a distinct front through the dense clusters.

Figure 4.4a presents the epidemic curves for the high transmissibility system with $\beta/\mu = 5.0$, as shown in Figure 4.3. In this case, all particles become infected ($s_\infty = 0$) regardless of the presence of obstacles. The peak value $i_{\max}$ is nearly identical for both scenarios. Interestingly, a noteworthy effect emerges: for $\tilde{t} < 0.175$, the addition of obstacles decreases the infected fraction i, while for $\tilde{t} > 0.185$, the presence of obstacles increases i. This phenomenon cannot be attributed solely to a change in the epidemic duration, as the curves are plotted in reduced time. Instead, it signifies a shift in the spatial propagation of the infection, which will be further addressed in Figures 4.6 and 4.7. The crossover in behavior occurs after the initial large infection front has fully propagated through either the giant cluster or all smaller clusters in the samples with quenched disorder. In Figure 4.4b, we plot the corresponding η versus $\tilde{t}$, which remains largely unaffected by the inclusion of obstacles. These findings indicate that under high transmissibility, the system exhibits reduced sensitivity to spatial disorder, aligning with the behavior observed in the mean field limit.

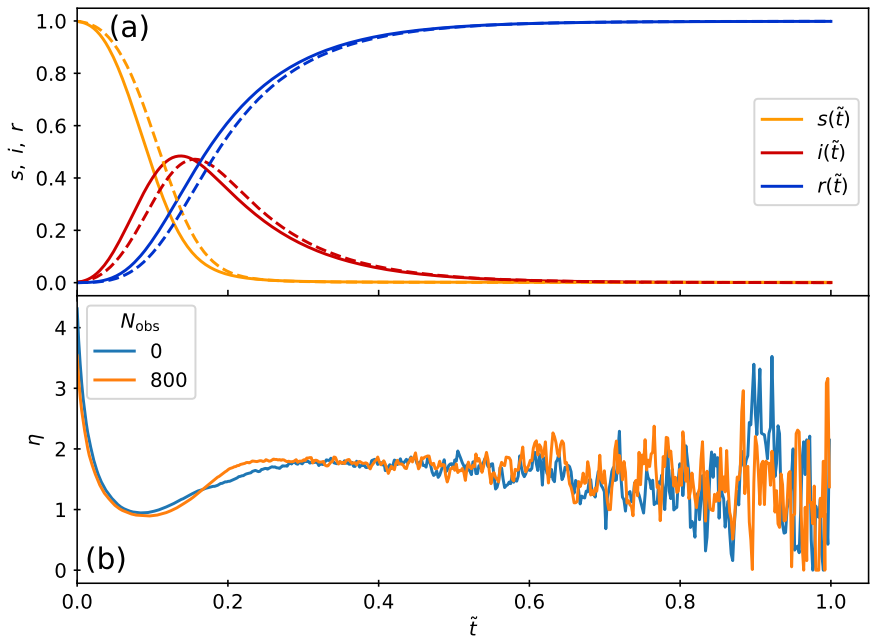

Figure 4.4: In panel (a), we present the epidemic curves for the high transmissibility regime. The curves represent the fractions of susceptible (s), infected (i), and recovered (r) particles as a function of reduced time ($\tilde{t}$) for the system shown in Figure 4.3 with $\beta/\mu = 5.0$. The solid lines correspond to samples without quenched disorder, while the dashed lines represent samples containing obstacles. In this scenario, all particles become infected, resulting in $s_\infty = 0$. Furthermore, panel (b) displays the average number of susceptible particles surrounding an infected particle, denoted as η, as a function of reduced time ($\tilde{t}$). The blue curve represents the sample without obstacles, while the orange curve represents the sample with obstacles. In this case, there is minimal difference in η between the two scenarios.

The epidemic curves and plots of $\eta(t)$ for all other β/μ can be viewed in Appendix A.

4.3 Duration of epidemic

Our simulations have revealed a significant level of stochasticity in the behavior of the epidemic. The duration of the epidemic, denoted as t_d, can vary greatly depending on the randomly chosen locations of the index cases. In some cases, the outbreak fails to establish and extinguishes without significantly affecting a substantial fraction of the particles.

To demonstrate this variability, we present the distribution $P(t_d)$ of the epidemics measured in simulation time steps, considering both scenarios with and without obstacles. In Figure 4.5, we specifically focus on the low transmissibility regime, examining cases with $\beta/\mu = 0.4$, 0.45, 0.5, 0.6, and 1.0. In this regime, the distribution exhibits a bimodal nature, indicating a clear distinction between small t_d values associated with failed outbreaks that do not impact a significant fraction of the particles, and larger t_d values corresponding to successful epidemics involving a substantial fraction of the population. This behavior aligns with observations from other studies [37].

The introduction of quenched disorder in this regime amplifies the likelihood of outbreak failure while also increasing the average duration of successful epidemics. However, in the high transmissibility regime, represented by $\beta/\mu = 2.0$ and 3.0 in Figures 4.5f and 4.5g, respectively, the distribution $P(t_d)$ becomes unimodal. Here, all outbreaks lead to successful epidemics, and the presence or absence of quenched disorder no longer exhibits a significant difference in the distribution.

4.4 Ability of I to contact S

We can differentiate between the two regimes of behavior by examining features in η, specifically by comparing the values of η in samples with and without quenched disorder. In Figure 4.6a, we present a plot of η against $\tilde{t}'$, where the time scale $\tilde{t}'$ represents the point at which the number of recovered individuals has reached 95% of its maximum value, $r(\tilde{t}' = 1.0) = 0.95 r_\infty = 0.95(1 - s_\infty)$. By using this time scale, we exclude the stochastic behavior observed at late times when only a few remaining infectives are recovering.

At $\tilde{t}' = 0$, η is consistently high since the initial seed I particles are surrounded exclusively by susceptible particles. As the epidemic spreads, the average number of susceptible (S) particles around infected (I) particles decreases. When $\beta/\mu \leq 1.5$, the curves exhibit a monotonic decrease, reaching a saturation value ranging from $\eta = 2.5$ to $\eta = 3.25$. Samples with obstacles consistently display lower values of η compared to those without obstacles.

For $\beta/\mu > 1.5$, the epidemic spreads in the form of a front, which is evident as a local dip in η centered around $\tilde{t}' = 0.2$. As the front rapidly moves through the largest cluster, most of the infected particles become surrounded by other infected particles behind the expanding front, leaving only those at the front edge adjacent to susceptible particles (S). This results in a decrease in the value of η. Once the front has passed through the cluster, the mobility of the particles brings more susceptible particles from the gas phase into contact with the

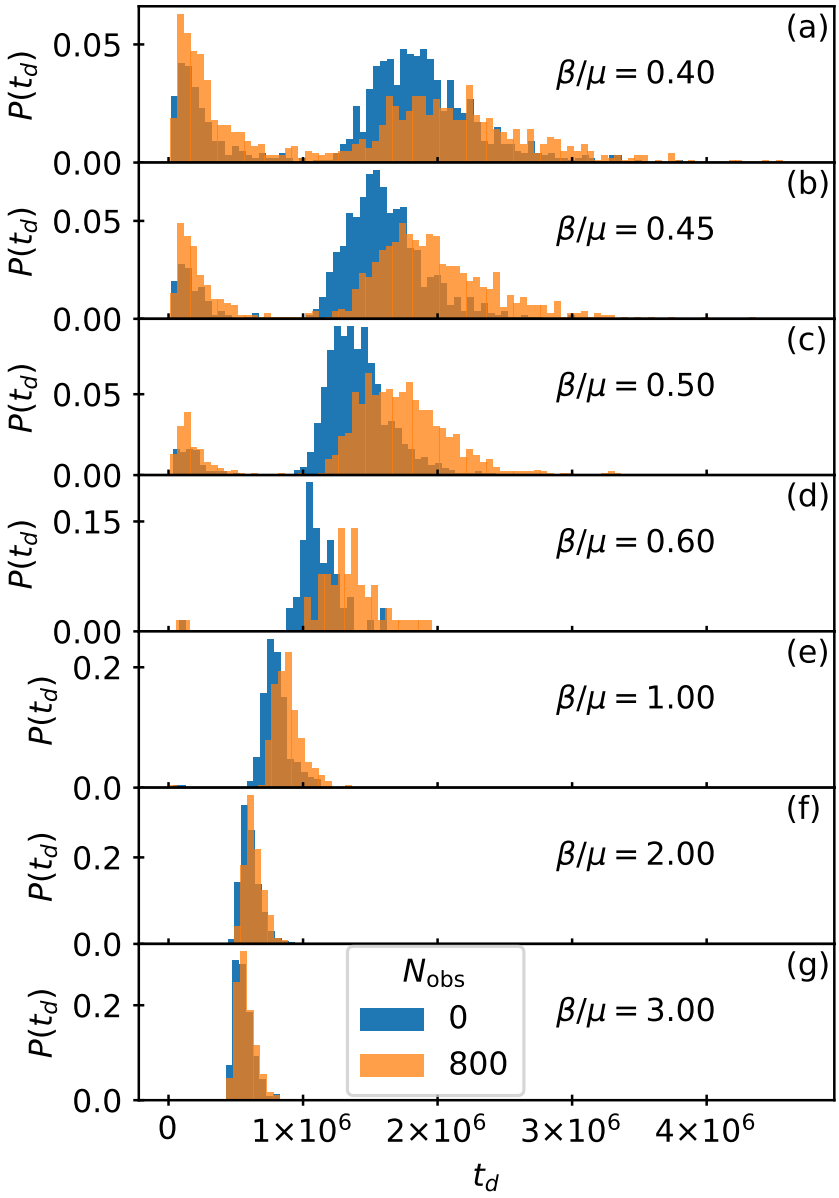

Figure 4.5: The durations of epidemics in the presence and absence of quenched disorder are examined in the low and high transmissibility regimes. The distribution $P(t_d)$ of epidemic durations, measured in simulation time steps, is illustrated for 1000 realizations. The blue curves represent systems without obstacles, while the orange curves represent systems with obstacles. The low transmissibility regime is characterized by $\beta/\mu=$ (a) 0.4, (b) 0.45, (c) 0.5, (d) 0.6, and (e) 1.0, while the high transmissibility regime is denoted by $\beta/\mu=$ (f) 2.0 and (g) 3.0. In the low transmissibility regime, the distributions (a-e) exhibit a bimodal nature, and the inclusion of quenched disorder leads to an increase in the number of failed outbreaks and prolongs the duration of successful epidemics. Conversely, in the high transmissibility regime (f,g), failed outbreaks are absent, and the impact of quenched disorder is significantly diminished.

remaining infected particles (I), leading to a partial recovery of η before it saturates at a low value between $\eta = 1.5$ and $\eta = 2.0$.

In Figure 4.6b, we present a plot of the difference, $\Delta\eta = \eta_{\text{obs=800}} - \eta_{\text{obs=0}}$, which represents

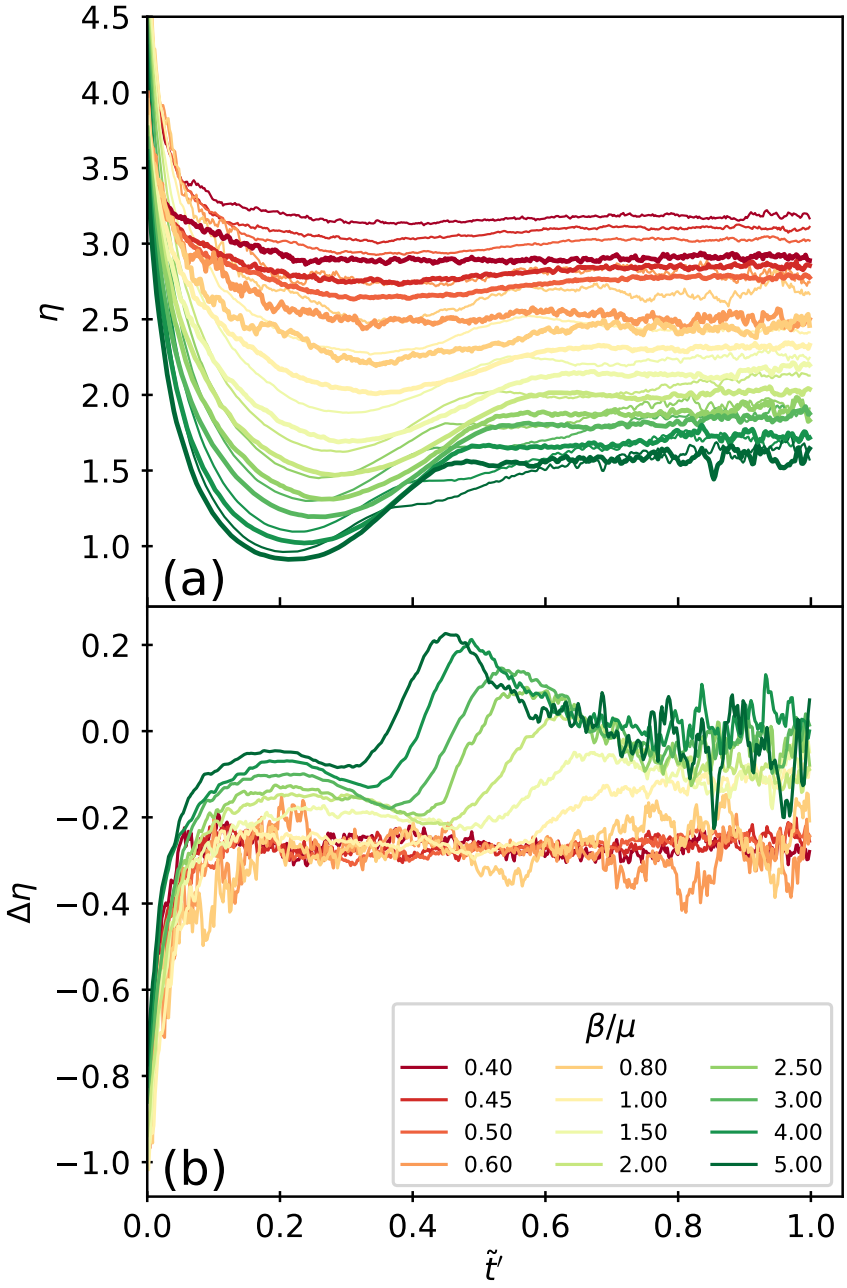

Figure 4.6: Measurement of the contact between infected (I) and susceptible (S) particles, and how it is influenced by the introduction of quenched disorder, is examined. (a) The plot shows η versus $\tilde{t}'$ for varied β/μ values. The thin lines represent samples without obstacles, while the thick lines represent samples with obstacles. In cases where β/μ is large, a local minimum in η is observed around $\tilde{t}' = 0.1$ due to the formation of a propagating front. (b) The difference, $\Delta\eta$, between the values of η in samples with and without disorder is plotted against $\tilde{t}'$. For $\beta/\mu \leq 1.5$, where no front propagation occurs, the addition of quenched disorder consistently reduces the value of η. However, for $\beta/\mu > 1.5$, when a front emerges, $\Delta\eta$ drops below zero after the front has passed, indicating an enhancement in the infection rate when quenched disorder is present.

the change in η between samples with and without quenched disorder from Figure 4.6a. When $\beta/\mu \leq 1.5$, $\Delta\eta$ reaches a constant negative value of approximately $\Delta\eta \approx -0.25$. This

indicates that the presence of quenched disorder consistently reduces the effectiveness of epidemic spread in this regime.

Once the system enters the front propagation regime for $\beta/\mu > 1.5$, $\Delta\eta$ exhibits a nonmonotonic behavior with local peaks and dips. For $\tilde{t}' < 0.4$, there is a dip when the front is passing through the largest clusters. In this case, $\Delta\eta$ is negative, suggesting that quenched disorder slows down the front to some extent. Beyond the minimum of the dip, $\Delta\eta$ increases and becomes positive, indicating that the addition of quenched disorder actually enhances the effectiveness of epidemic spread. This observation aligns with Figure 4.4a, where the presence of quenched disorder reduces the number of infected individuals (i) for $\tilde{t}' < 0.175$ but slightly increases it for $\tilde{t}' > 0.175$. This indicates that disorder can accelerate the infection at later times.

The enhancement of the epidemic occurs after the largest cluster has become fully infected, and some infected particles break away from the cluster and enter the gas phase. Within the gas phase, the quenched disorder induces the formation of smaller localized clusters, as depicted in Figure 2.1. These smaller clusters, upon contact with an infective, undergo the same rapid front propagation as the initial wave of infection. In contrast, when quenched disorder is absent, there are no smaller clusters, and the infection must propagate through the gas phase, infecting the remaining susceptible (S) particles one by one, which is an inefficient process.

4.5 Epidemic phase diagram

Based on the observed characteristics in Figure 4.6, we can create a phase diagram to illustrate the system's behavior as a function of β/μ versus $\tilde{t}'$. This phase diagram is shown in Figure 4.7. When $\beta/\mu > 1.5$, the entire system becomes infected ($s_\infty = 0$), and the initial spread of the infection occurs through front propagation. In the regime marked as FP (front propagation), the infection spreads via a front through the largest cluster. The addition of quenched disorder in this regime can slow down the front propagation but does not halt it. Once the front has passed through the entire largest cluster, the system enters the CP (secondary cluster propagation) regime, where secondary clusters start exhibiting front propagation. In this regime, the presence of quenched disorder can enhance the spread of the infection by increasing the number of secondary clusters. At larger values of $\tilde{t}'$, all clusters have been infected, and the epidemic progresses through the gas phase. This regime is referred to as Diff (diffusive), where there is minimal difference between systems with and without quenched disorder.

For $\beta/\mu \leq 1.5$, which corresponds to the low transmissibility regime (marked as LT), the infection spreads more uniformly, as depicted in Figure 4.1. In this regime, $s_\infty > 0$, meaning not all particles are infected by the end of the epidemic. The addition of quenched disorder consistently reduces the maximum number of infected particles ($i_{\max}$) and increases s_∞.

It is worth noting that the phase boundaries in the phase diagram may depend on factors

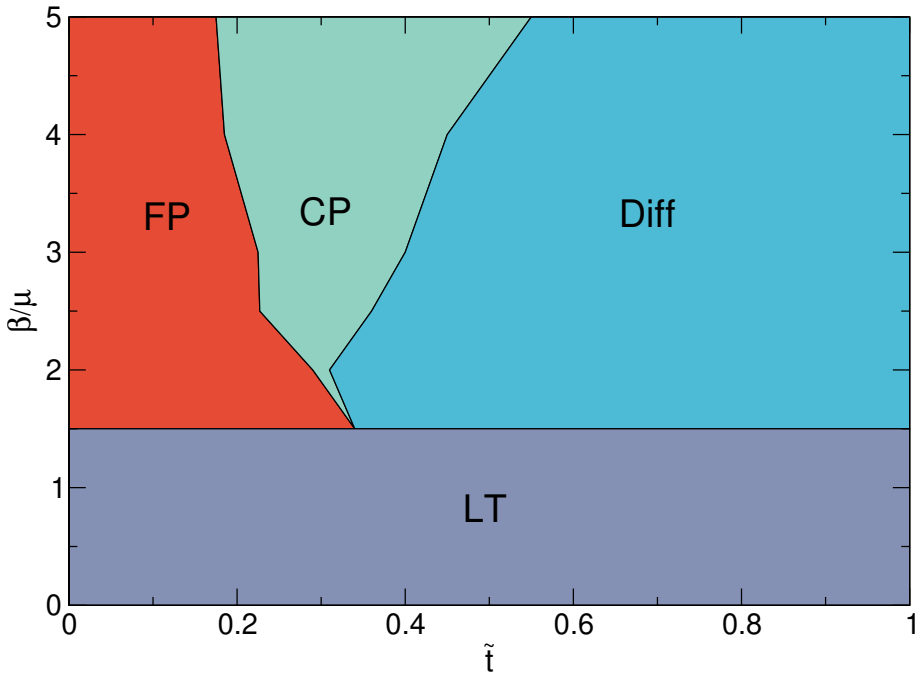

Figure 4.7: The phase diagram illustrates the evolution of the epidemic in both low and high transmissibility regimes. It is presented as a function of transmissibility β/μ versus reduced time $\tilde{t}'$. In the low transmissibility (LT) regime, characterized by $\beta/\mu \leq 1.5$, the system exhibits $s_\infty > 0$, indicating that a fraction of susceptible particles remains unaffected by the epidemic. The presence of obstacles has a significant impact on the propagation of the epidemic in this regime. The front propagation phase (FP) occurs in the high transmissibility regime, where the infection spreads rapidly through the system. This phase is marked by efficient transmission and a prominent propagating front. The addition of obstacles may still influence the spread of the infection, but to a lesser extent compared to the low transmissibility regime. In the secondary cluster phase (CP), obstacles can actually enhance the spread of the infection. This phase is characterized by the formation of secondary clusters that contribute to the overall epidemic propagation. The obstacles facilitate the clustering effect, leading to increased infection transmission. The diffusive regime (Diff) is characterized by a more uniform and diffusive spread of the infection. In this regime, the presence of obstacles has minimal impact on the epidemic spread.

such as the amount of quenched disorder and the activity level of the particles.

4.6 Effect of changing quenched disorder density

To examine the resilience of our findings to variations in the density of quenched disorder sites, we present in Figures 4.8a–g the distribution $P(t_d)$ of epidemic durations in a sample with $N_{\text{obs}} = 1600$ obstacles. In the low transmissibility regime, the presence of obstacles further suppresses successful outbreaks as the obstacle density increases. This occurs because the formation of large clusters, observed at lower obstacle densities, gets disrupted when the obstacle density rises, as demonstrated in Figure 4.8i. On the other hand, in the high transmissibility regime characterized by $\beta/\mu \geq 2$, even with a higher number of quenched disorder sites, the impact on outbreak duration remains negligible. Therefore, our observation that quenched disorder loses significance in the context of high transmissibility remains

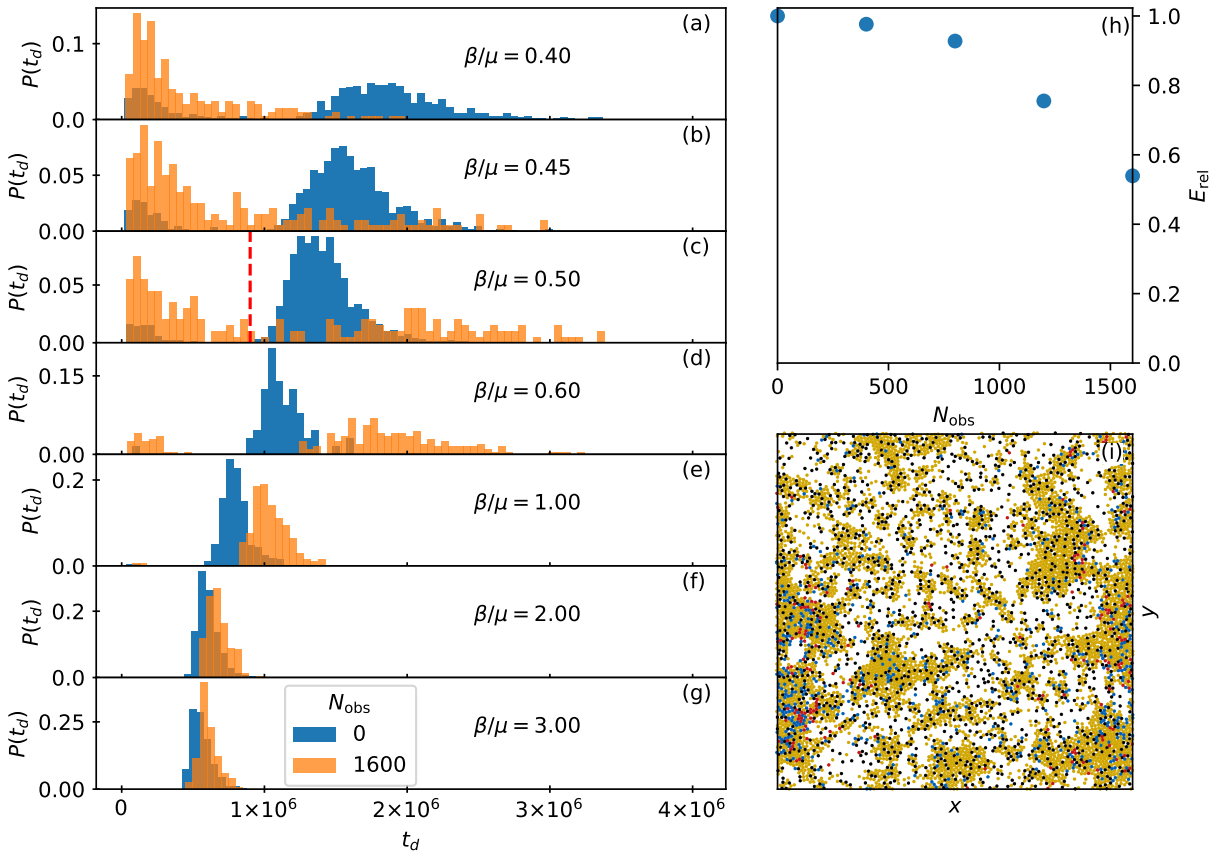

Figure 4.8: Impact of varying quenched disorder density can be observed in the following manner. Panels (a–g) present the distribution $P(t_d)$ of epidemic duration t_d in simulation time steps, encompassing 200 realizations. Blue curves represent systems without obstacles, while orange curves represent systems with $N_{\text{obs}} = 1600$ obstacles. The scenarios covered include both low and high transmissibility regimes: $\beta/\mu =$ (a) 0.4, (b) 0.45, (c) 0.5, (d) 0.6, (e) 1.0, (f) 2.0, and (g) 3.0. Similar to the case with fewer obstacles, there are no failed outbreaks in the high transmissibility regime, leading to a notable reduction in the effect of quenched disorder. Panel (h) displays the relative fraction E_{rel} of successful outbreaks in the presence of quenched disorder compared to the absence of quenched disorder, specifically for systems with different numbers of obstacles N_{obs} at $\beta/\mu = 0.5$. The dashed line in panel (c) indicates the threshold used to distinguish failed and successful outbreaks when calculating E_{rel}. In panel (i), an image snapshot of the epidemic is presented for a system with $N_{\text{obs}} = 1600$ and $\beta/\mu = 0.5$ at the peak of the infection. The susceptible (S) particles are depicted in yellow, infected (I) particles in red, and recovered (R) particles in blue. The increased density of quenched disorder sites has caused the system to fragment into numerous smaller clusters.

consistent as the number of obstacles increases.

To quantify the influence of quenched disorder in the low transmissibility regime with $\beta/\mu = 0.5$, we measure the total number of outbreaks (E_s) within the successful window. The successful window consists of outbreaks with durations (t_d) that exceed the threshold indicated by the red dashed line in Figure 4.8c. By comparing the number of outbreaks

in samples with quenched disorder (E_s^{obs}) to the number of outbreaks in samples without quenched disorder (E_s^0), we calculate the relative fraction of successful outbreaks, denoted as $E_{\text{rel}} = E_s^{\text{obs}}/E_s^0$. Figure 4.8h illustrates the relationship between E_{rel} and N_{obs}, revealing that as the density of obstacles (N_{obs}) increases, there is a greater suppression of successful outbreaks in comparison to the disorder-free system. It is worth noting that if the obstacle density becomes so high that the obstacles begin to percolate across the sample, causing it to split into disconnected regions, E_{rel} could potentially drop to zero. However, further investigation into this regime will be addressed in future research.

The duration of epidemics for $N_{\text{obs}} = 400$ and 1200 can be viewed in Appendix B.

Conclusions

Our model suggests that active matter systems offer a versatile approach to studying various epidemic behaviors. One such system is active colloids, where the activity of individual particles can be controlled using optical rastering techniques. These systems have been utilized in experiments to replicate group formation, simulate visual perception mobility, and generate collective behaviors like quorum sensing [1, 19].

To implement an S-I-R model, individual active colloids can be tracked and labeled based on their infective state, and when they interact with other colloids, there can be a probability of transmitting the infection to susceptible ones. This can be achieved in a motility-induced phase-separated regime or a diffusive regime with varying β/μ. The experiments can be repeated multiple times to obtain average behavior. In a given sample, certain colloids can remain inactive and be considered as passive or obstacle particles, or physical obstacles can be introduced on the substrate.

Moreover, additional rules can be incorporated, such as hyperactive particles acting as superspreaders or potential mitigation effects. This approach has the potential to position active matter as a tabletop experimental system for modeling epidemics. Our findings highlight that active matter can serve as a simulation tool for studying epidemics in a system that can be easily tuned between states sensitive and insensitive to spatial disorder.

In summary, we have demonstrated the utilization of an active matter system consisting of self-propelled particles to simulate spatial heterogeneity within an S-I-R epidemic spreading model. The inherent clustering behavior of the active particles emerges naturally in the motility-induced phase-separated regime. In the low transmissibility regime, characterized by percolative epidemic spread, the system exhibits sensitivity to the introduction of quenched disorder. This leads to an increased likelihood of failed outbreaks and longer average durations of successful epidemics. Consequently, the classical mixing hypothesis of traditional S-I-R models is no longer applicable in this regime. On the other hand, in the high transmissibility regime, where all particles eventually get infected and the epidemic propagates through well-defined fronts, the addition of quenched disorder initially slows down the spread by impeding the propagation of the initial front. However, at later stages, the presence of quenched disorder facilitates more efficient epidemic spreading due to the emergence of numerous small clusters in the gas phase. Our findings highlight the impact of spatial disorder on epidemic spread across both high and low transmissibility regimes.

The proposed system can be potentially realized experimentally using light-activated

colloidal particles controlled by specific feedback rules to mimic the S-I-R model. These results suggest that active matter systems offer a promising avenue for conducting table-top epidemic experiments.

Appendix A

Epidemic curves

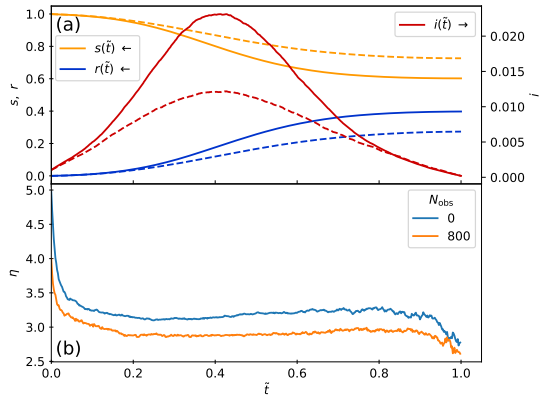

(a) Epidemic curves in the low transmissibility regime ($\beta/\mu = 0.40$).

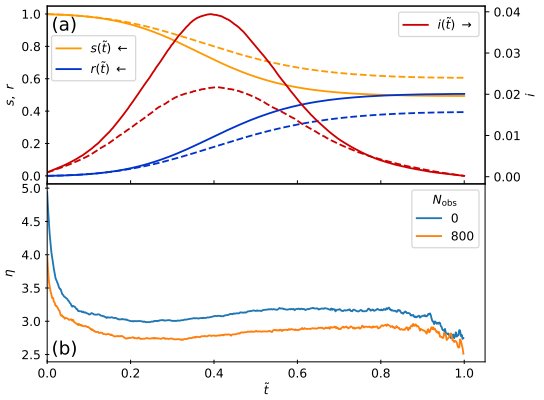

(b) Epidemic curves in the low transmissibility regime ($\beta/\mu = 0.45$).

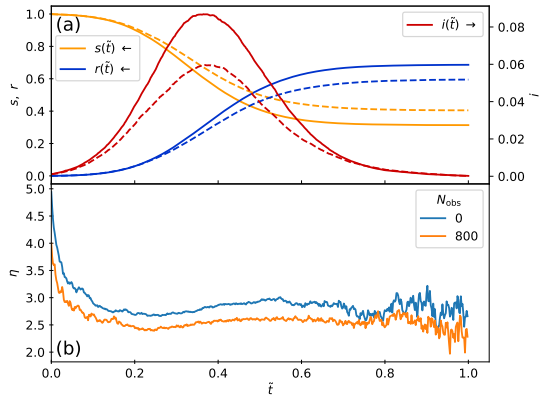

(c) Epidemic curves in the low transmissibility regime ($\beta/\mu = 0.60$).

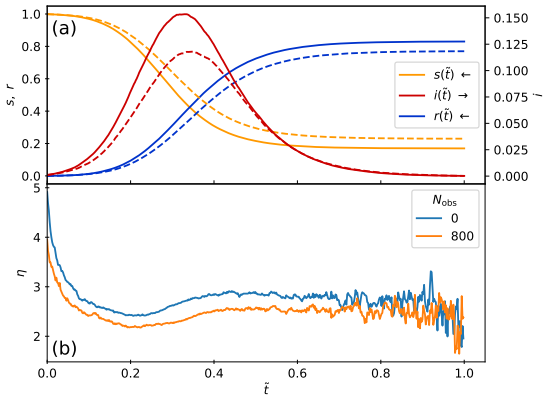

(d) Epidemic curves in the low transmissibility regime ($\beta/\mu = 0.80$).

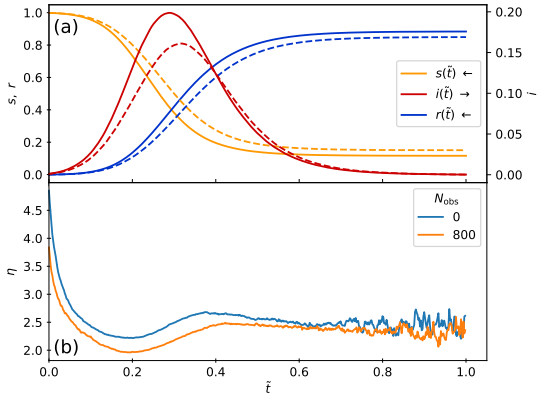

(e) Epidemic curves in the low transmissibility regime ($\beta/\mu = 1.00$).

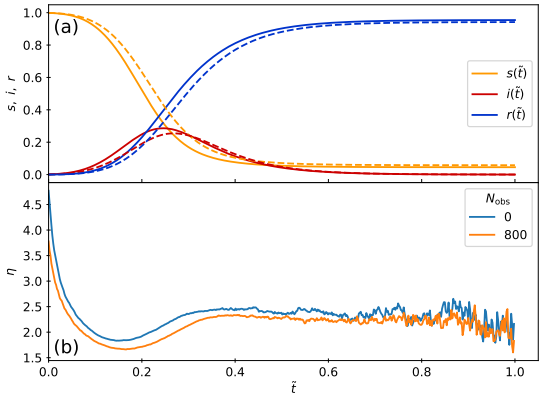

(f) Epidemic curves in the transitional transmissibility regime ($\beta/\mu = 1.50$).

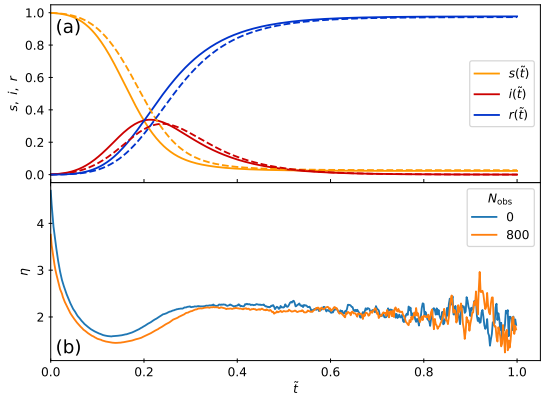

(g) Epidemic curves in the high transmissibility regime ($\beta/\mu = 2.00$).

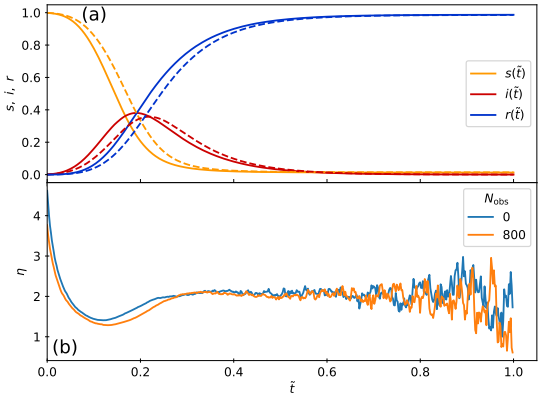

(h) Epidemic curves in the high transmissibility regime ($\beta/\mu = 2.50$).

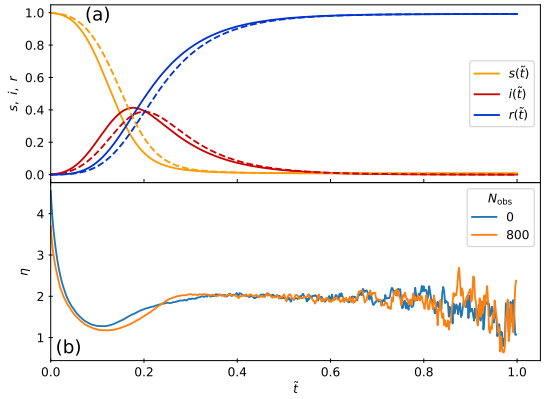

(i) Epidemic curves in the high transmissibility regime ($\beta/\mu = 3.00$).

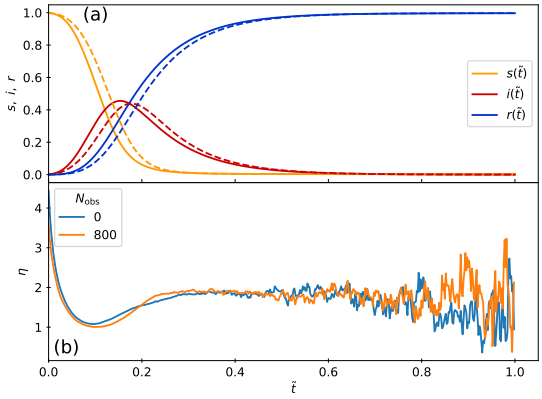

(j) Epidemic curves in the high transmissibility regime ($\beta/\mu = 4.00$).

Figure A.1: (a) The system's evolution of $s(\tilde{t})$ (represented in yellow), $i(\tilde{t})$ (represented in red), and $r(\tilde{t})$ (represented in blue) is depicted for a system. Solid lines represent samples without quenched disorder, while dashed lines correspond to samples containing obstacles ($N_{\text{obs}} = 800$). (b) The corresponding $\eta(\tilde{t})$ values are shown in blue for systems without obstacles and in orange for systems with obstacles.

Appendix B

Duration of epidemic for different obstacle densities

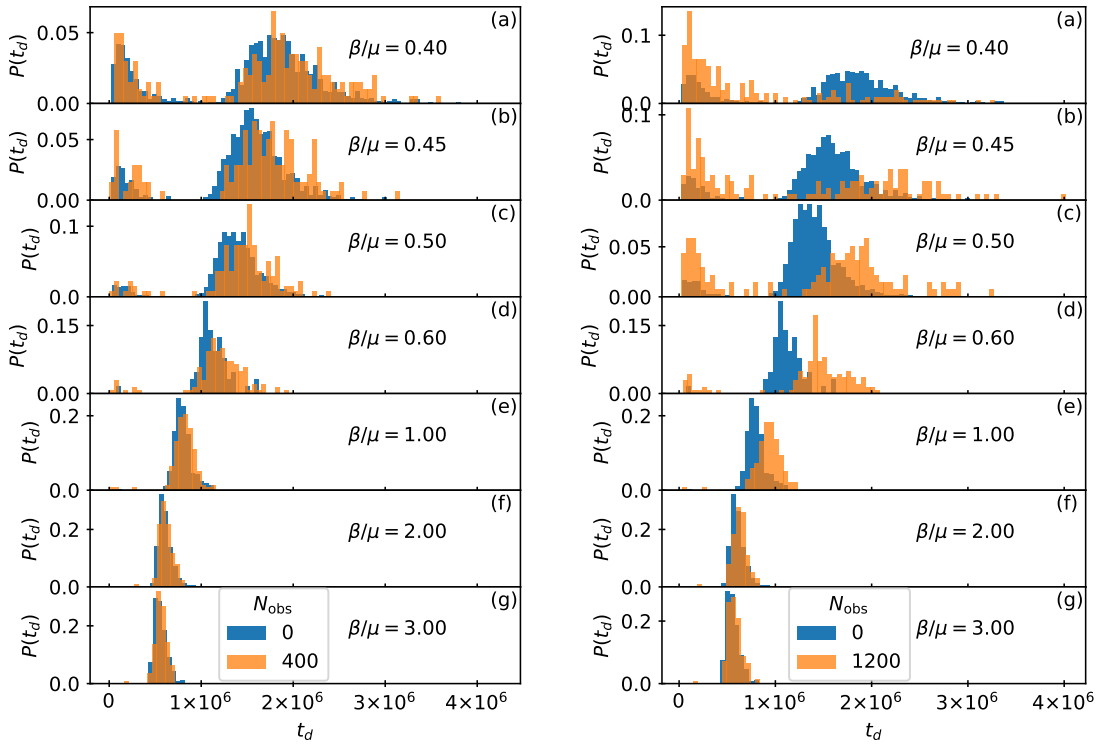

(a) $N_{\text{obs}} = 400$ (b) $N_{\text{obs}} = 1200$

Figure B.1: The durations of epidemics in the presence and absence of quenched disorder are examined in the low and high transmissibility regimes. The distribution $P(t_d)$ of epidemic durations, measured in simulation time steps, is illustrated for 200 realizations. The blue curves represent systems without obstacles, while the orange curves represent systems with obstacles.

Bibliography

[1] Tobias Bäuerle, Robert C Löffler, and Clemens Bechinger. Formation of stable and responsive collective states in suspensions of active colloids. *Nature Communications*, 11(1):2547, 2020.

[2] Clemens Bechinger, Roberto Di Leonardo, Hartmut Löwen, Charles Reichhardt, Giorgio Volpe, and Giovanni Volpe. Active particles in complex and crowded environments. *Reviews of Modern Physics*, 88(4):045006, 2016.

[3] Tapomoy Bhattacharjee and Sujit S Datta. Bacterial hopping and trapping in porous media. *Nature communications*, 10(1):2075, 2019.

[4] N Boccara and K Cheong. Automata network sir models for the spread of infectious diseases in populations of moving individuals. *Journal of Physics A: Mathematical and General*, 25(9):2447, 1992.

[5] Arturo Buscarino, Luigi Fortuna, Mattia Frasca, and Vito Latora. Disease spreading in populations of moving agents. *Europhysics Letters*, 82(3):38002, 2008.

[6] Michael E Cates and Julien Tailleur. Motility-induced phase separation. *Annu. Rev. Condens. Matter Phys.*, 6(1):219–244, 2015.

[7] Chun-Jen Chen and Clemens Bechinger. Collective response of microrobotic swarms to external threats. *New Journal of Physics*, 24(3):033001, 2022.

[8] Stephen Eubank, Hasan Guclu, VS Anil Kumar, Madhav V Marathe, Aravind Srinivasan, Zoltan Toroczkai, and Nan Wang. Modelling disease outbreaks in realistic urban social networks. *Nature*, 429(6988):180–184, 2004.

[9] Paul Fenimore, Benjamin McMahon, Nicolas Hengartner, Timothy Germann, and Judith Mourant. A suite of mechanistic epidemiological decision support tools. *Online Journal of Public Health Informatics*, 10(1), 2018.

[10] Yaouen Fily and M Cristina Marchetti. Athermal phase separation of self-propelled particles with no alignment. *Physical review letters*, 108(23):235702, 2012.

[11] P Forgács, A Libál, C Reichhardt, N Hengartner, and CJO Reichhardt. Using active matter to introduce spatial heterogeneity to the susceptible infected recovered model of epidemic spreading. *Scientific Reports*, 12(1):11229, 2022.

[12] Mattia Frasca, Arturo Buscarino, Alessandro Rizzo, Luigi Fortuna, and Stefano Boccaletti. Dynamical network model of infective mobile agents. *Physical Review E*, 74(3):036110, 2006.

[13] Daan Frenkel and Berend Smit. *Understanding molecular simulation: from algorithms to applications*, volume 1. Elsevier, 2001.

[14] Timothy C Germann, Kai Kadau, Ira M Longini Jr, and Catherine A Macken. Mitigation strategies for pandemic influenza in the united states. *Proceedings of the National Academy of Sciences*, 103(15):5935–5940, 2006.

[15] Herbert W Hethcote. The mathematics of infectious diseases. *SIAM review*, 42(4):599–653, 2000.

[16] Matthew J Keeling. The effects of local spatial structure on epidemiological invasions. *Proceedings of the Royal Society of London. Series B: Biological Sciences*, 266(1421):859–867, 1999.

[17] William Ogilvy Kermack and Anderson G McKendrick. A contribution to the mathematical theory of epidemics. *Proceedings of the royal society of london. Series A, Containing papers of a mathematical and physical character*, 115(772):700–721, 1927.

[18] Alejandro B Kolton and Karina Laneri. Rough infection fronts in a random medium. *The European Physical Journal B*, 92:1–11, 2019.

[19] François A Lavergne, Hugo Wendehenne, Tobias Bäuerle, and Clemens Bechinger. Group formation and cohesion of active particles with visual perception–dependent motility. *Science*, 364(6435):70–74, 2019.

[20] Celia Lozano, Borge Ten Hagen, Hartmut Löwen, and Clemens Bechinger. Phototaxis of synthetic microswimmers in optical landscapes. *Nature communications*, 7(1):12828, 2016.

[21] Pierre Magal and Shigui Ruan. Susceptible-infectious-recovered models revisited: From the individual level to the population level. *Mathematical biosciences*, 250:26–40, 2014.

[22] M Cristina Marchetti, Jean-François Joanny, Sriram Ramaswamy, Tanniemola B Liverpool, Jacques Prost, Madan Rao, and R Aditi Simha. Hydrodynamics of soft active matter. *Reviews of modern physics*, 85(3):1143, 2013.

[23] Joel C Miller. Epidemic size and probability in populations with heterogeneous infectivity and susceptibility. *Physical Review E*, 76(1):010101, 2007.

[24] Joel C Miller. A note on the derivation of epidemic final sizes. *Bulletin of mathematical biology*, 74(9):2125–2141, 2012.

[25] Ariel Norambuena, Felipe J Valencia, and Francisca Guzmán-Lastra. Understanding contagion dynamics through microscopic processes in active brownian particles. *Scientific Reports*, 10(1):20845, 2020.

[26] Kristian S Olsen, Luiza Angheluta, and Eirik G Flekkøy. Active brownian particles moving through disordered landscapes. *Soft Matter*, 17(8):2151–2157, 2021.

[27] Jeremie Palacci, Stefano Sacanna, Asher Preska Steinberg, David J Pine, and Paul M Chaikin. Living crystals of light-activated colloidal surfers. *Science*, 339(6122):936–940, 2013.

[28] Matteo Paoluzzi, Marco Leoni, and M Cristina Marchetti. Information and motility exchange in collectives of active particles. *Soft Matter*, 16(27):6317–6327, 2020.

[29] Romualdo Pastor-Satorras, Claudio Castellano, Piet Van Mieghem, and Alessandro Vespignani. Epidemic processes in complex networks. *Reviews of modern physics*, 87(3):925, 2015.

[30] Fernando Peruani and Gustavo J Sibona. Dynamics and steady states in excitable mobile agent systems. *Physical review letters*, 100(16):168103, 2008.

[31] Fernando Peruani and Gustavo J Sibona. Reaction processes among self-propelled particles. *Soft matter*, 15(3):497–503, 2019.

[32] Erçağ Pinçe, Sabareesh KP Velu, Agnese Callegari, Parviz Elahi, Sylvain Gigan, Giovanni Volpe, and Giorgio Volpe. Disorder-mediated crowd control in an active matter system. *Nature communications*, 7(1):10907, 2016.

[33] Dennis C Rapaport and Dennis C Rapaport Rapaport. *The art of molecular dynamics simulation*. Cambridge university press, 2004.

[34] Gabriel S Redner, Michael F Hagan, and Aparna Baskaran. Structure and dynamics of a phase-separating active colloidal fluid. *Physical review letters*, 110(5):055701, 2013.

[35] C Reichhardt and CJ Olson Reichhardt. Active matter transport and jamming on disordered landscapes. *Physical Review E*, 90(1):012701, 2014.

[36] Steven Riley, Ken Eames, Valerie Isham, Denis Mollison, and Pieter Trapman. Five challenges for spatial epidemic models. *Epidemics*, 10:68–71, 2015.

[37] Kat Rock, Sam Brand, Jo Moir, and Matt J Keeling. Dynamics of infectious diseases. *Reports on Progress in Physics*, 77(2):026602, 2014.

[38] Jorge P Rodríguez, Fakhteh Ghanbarnejad, and Víctor M Eguíluz. Particle velocity controls phase transitions in contagion dynamics. *Scientific reports*, 9(1):6463, 2019.

[39] Cs Sándor, Andras Libal, Charles Reichhardt, and CJ Olson Reichhardt. Dynamic phases of active matter systems with quenched disorder. *Physical Review E*, 95(3):032606, 2017.

[40] Gui-Quan Sun, Marko Jusup, Zhen Jin, Yi Wang, and Zhen Wang. Pattern transitions in spatial epidemics: Mechanisms and emergent properties. *Physics of life reviews*, 19:43–73, 2016.

[41] Michael Te Vrugt, Jens Bickmann, and Raphael Wittkowski. Effects of social distancing and isolation on epidemic spreading modeled via dynamical density functional theory. *Nature communications*, 11(1):5576, 2020.

[42] Óscar Toledano, Begoña Mula, Silvia N Santalla, Javier Rodríguez-Laguna, and Óscar Gálvez. Effects of confinement and vaccination on an epidemic outburst: A statistical mechanics approach. *Physical Review E*, 104(3):034310, 2021.

[43] Loup Verlet. Computer" experiments" on classical fluids. i. thermodynamical properties of lennard-jones molecules. *Physical review*, 159(1):98, 1967.

[44] Erik Volz and Lauren Ancel Meyers. Susceptible–infected–recovered epidemics in dynamic contact networks. *Proceedings of the Royal Society B: Biological Sciences*, 274(1628):2925–2934, 2007.

[45] Yinong Zhao, Cristián Huepe, and Pawel Romanczuk. Contagion dynamics in self-organized systems of self-propelled agents. *Scientific reports*, 12(1):2588, 2022.